Hypersonic wake velocity measurements using acetone molecular tagging velocimetry

Angelina Andrade[1], Chad O. Willamson[1], Nicholas W. Stegmeier[1], Kevin R. Posladek[1], Nathan S. Strasser[1], and Christopher S. Combs[2]
The University of Texas at San Antonio, San Antonio, Texas, 78249, US

W. Lawton Shoemake[3], Christopher L. Hall[4], Kristopher T. Olshefski[5], Nicole F. Nutter [1], Ryan S. Glasby[6]
Oak Ridge National Laboratory, Oak Ridge, Tennessee, 37830, US

A non-intrusive laser diagnostic known as molecular tagging velocimetry was used to find quantitative off-body velocity measurements in the wake of a sphere in the Mach 7 Ludwieg Tube Wind Tunnel located at The University of Texas at San Antonio. Acetone gas seeded in the flow was excited using the 4th harmonic of a pulse-burst Nd:YAG laser. The experimental results were used to validate and compare to simulations using a continuous Galerkin flow solver. Both the experimental and simulated results agreed on negative velocities in the viscous shear layer. Near the centerline of the sphere, average velocities of -200 m/s were observed due to reverse flow in the recirculation region. Outside of the shear layer, velocities of 800 m/s were observed in both the experimental and simulated results. The overall average uncertainty for the strut-mounted and free-flight case was estimated to be ±27 m/s. The flow features of the wake were visualized using schlieren imaging, and the experimental results agreed well with the simulated results.

I. Nomenclature

M	=	Mach number
Re	=	unit Reynolds number, m^{-1}
Re_d	=	Reynolds number based on diameter
d	=	diameter, m
Δt	=	time delay, ns
P_0	=	stagnation pressure, MPa
T_0	=	stagnation temperature, K

[1] Graduate Research Assistant, Department of Mechanical Engineering, AIAA Student Member.
[2] Dee Howard Endowed Associate Professor, Department of Mechanical Engineering, AIAA Senior Member.
[3] Scientific Software Engineer, AIAA Member.
[4] Research Scientist, AIAA Member.
[5] Computational Scientist, AIAA Member.
[6] Senior Research Scientist, AIAA Senior Member.

μ_0 = stagnation viscosity, $kg/m \cdot s$
P = static pressure in test section, kPa
u_∞ = freestream velocity, m/s
a_∞ = freestream speed of sound, m/s
T_∞ = freestream temperature, K
μ_∞ = freestream viscosity, $kg/m \cdot s$
ρ_∞ = freestream density, kg/m^3
C = Sutherland's constant for air
u_{rms} = velocity root mean square, m/s
u'_{rms} = turbulence root mean square, m/s

II. Introduction

The wake behind bodies has always been of interest in the aerodynamics community, more specifically in the re-entry of hypervelocity bodies, and has been extensively studied in previous literature [1,2]. Understanding the near wake and far wake flow structures behind a body has been critical in the design of aerodynamically stable planetary entry vehicles [3]. Wakes are generated by the distortion of the flow around a body as it moves through the fluid. As a body moves through a supersonic or hypersonic flow, the boundary layer of the body generates a viscous shear layer separating the inner flow and outer flow of the wake [4,5,6]. The inner flow consists of recirculating flow with strong velocity gradients, and the formation of a separation or "lip" shock is created by the separation of the boundary layer from the body [4]. The viscous shear layer then begins to decelerate and heat the flow as it converges to the "neck" of the wake and recompression waves begin to form a recompression shock downstream of the "neck" of the wake [1,4]. Accurate measurements of the flow field properties in hypersonic flow can be challenging due to pressure, temperature, and short test time environments associated with ground-testing facilities. Intrusive instrumentation such as hot-wire anemometers and Pitot probes have been used to characterize hypersonic flow properties, but they can physically disturb the flow [7].

In the past, intrusive instrumentation has been used to map the velocity of the flow structures associated with the wake behind a body [8,9]. Hot-wire anemometers have been used to collect measurements in the near wake by Todisco and Pallone [10] and in the far wake by Beherns [11]. In the far wake study, the wake of a circular cylinder demonstrated the decrease of the static temperature for a Mach 6 flow [11]. The near wake study concluded that the stagnation temperature in a Mach 16 flow for a 10° half-angle cone and a 10° half-angle wedge is highly influenced by the Reynolds number and the ratio between the wall and stagnation temperature [10]. Pitot probes have also been used as an intrusive technique to collect measurements in near wakes. Dewey investigates the near wake of a blunt body with the use of a Pitot probe, which resulted in a maximum pressure at the "neck" of the wake where the viscous shear layer converges [12]. Pitot probes have also been used to observe the near wake of 10° cones, where Murman found that the maximum static pressure is significantly greater than the freestream pressure of the flow [13]. The "lip" shock of a 6° half-angle wedge has also been investigated using a Pitot probe which resulted in an increase of the lip-shock strength as the Mach number increased [14]. As mentioned before, these types of intrusive techniques tend to alter the characteristics of the flow properties as seen in the measurements obtained in the recirculation region studied by Zakkay and Cresci [15]. Therefore, non-intrusive laser techniques have grown in popularity as they do not inherently disturb the flow structures in the wake of a body.

Laser doppler velocimetry (LDV) is one of the first laser techniques used to investigate wakes by Herrin and Dutton [16,17]. Since Pitot probes changed the fluid properties when measuring the recirculation region, Herrin and Dutton obtained mean and turbulent velocity profiles using LDV, of the recirculating region and the shear layer of the wake behind a circular cylinder at Mach 2.5 [16,17]. The most common laser diagnostic used in measuring the flow properties in a wake is planar laser induced fluorescence (PLIF) [18,19,20]. Lachney and Clemens measured the temperature and pressure fields of the wake of a flat plate at Mach 3 using nitric oxide as the seed gas and found lower pressures and temperatures (compared to the freestream temperature) in the expansion region [21]. The shear layer region of a wake has also been investigated by Combs et al. using PLIF at various angles of attack and surface roughness caused by ablation on the NASA's Orion Multi-Purpose Crew Vehicle at Mach 5 [22]. Particle image velocimetry (PIV) is another laser-based technique that has been used by Humble et al. and Scarano and Oudheusden at Mach 2 and described and unsteady behavior associated with the recompression shock leading to an increase of velocity fluctuations [23,24]. Bathel et al. found velocity measurements in the wake of cylinder trip on a flat plate using nitric oxide molecular tagging velocimetry (MTV) and witnessed lower velocity values in the wake of the trip relative to the pre-trip velocities [25]. Most recently, femtosecond laser electronic excitation tagging (FLEET) velocimetry was used to measure the velocity flow fields of a hypersonic wake behind a 7° half-angle cone [26].

This paper presents non-intrusive quantitative off-body velocity measurements in a hypersonic wake of a representative body in free-flight using acetone MTV to compare to and validate computational fluid dynamics (CFD) simulations. The velocity measurements obtained from free-flight tests are also compared to models strut-mounted to the facility's test section floor used in this study. Previous freestream and boundary layer measurements using acetone MTV by Andrade et al., have successfully been collected in a hypersonic facility [27]. Schlieren visualization of a sphere in free-flight versus strut-mounted has been used to observe the flow structures associated with a hypersonic wake. The fluid flow structures, and velocity measurements obtained in the experimental campaign were compared to simulations using an adaptive mesh CFD approach.

III. Experimental Program

A. Wind Tunnel Facility

The Mach 7.2 Ludwieg Wind Tunnel facility located at the University of Texas at San Antonio, depicted in Figure 1, was used in this experimental campaign. A 304 mm × 304 mm aluminum diaphragm separates the high- and low-pressure regions of the wind tunnel. In the high-pressure region, an 18-m-long driver tube provides stagnation pressures and temperatures of up to 14 MPa and 700 K, respectively. For this study, the driver tube was pressurized with air as the working fluid and operated at ambient temperature conditions to avoid any possibilities of ignition. The low-pressure region consists of a 6 m^3 (1600 gallons) vacuum tank coupled with a constant 203 mm × 203 mm (8 in × 8 in) cross-sectional test section with optical access on the wind tunnel sidewalls, ceiling, and floor. Once the flow commences from the rupture of the diaphragm, the facility offers test times of up to 500 ms, consisting of multiple steady-state passes of approximately 50 – 100 ms each. The facility produces Reynolds numbers between Re = 0.5 – 200 × 10^6 m^{-1} and an average freestream velocity of 886 m/s [27]. The hypersonic facility is capable of mounting models on a strut to the test section floor or releasing models to obtain free-flight conditions. A characterization of the facility's flow properties can be found in reference [28].

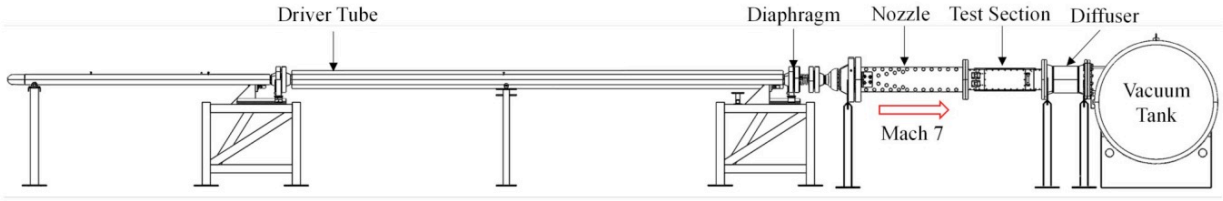

Figure 1. Wind Tunnel Facility.

B. Model Geometry

Spheres were chosen to generate wakes in this study as they are a relatively simple geometry that has been consistently studied and used to validate experimental techniques for decades [29-32]. In this study, two spheres with different diameters were either strut-mounted or released via a free-flight system. The free-flight models consisted of Nylon 25.4 mm (1 in) diameter spheres weighing approximately 9.64 grams each. Figure 2 demonstrates the Nylon sphere used for free-flight experiments. For the strut-mounted experiments, a stainless-steel sphere with a 50.8 mm (2 in) diameter was used.

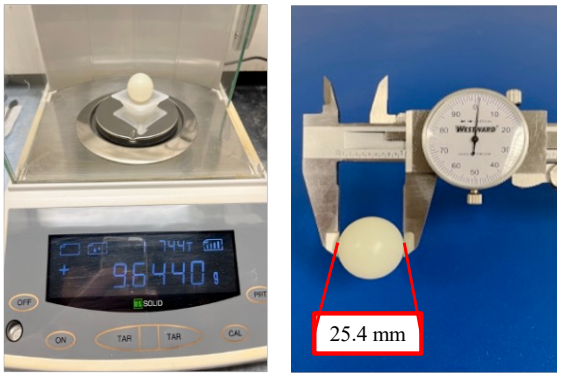

Figure 2. Free-flight model weight and size.

C. Experimental Setup

1. Schlieren Imaging

Schlieren imaging was used as a non-intrusive technique to visualize the hypersonic wake structures behind the sphere in strut-mounted and in free-flight configurations. This qualitative technique provides a visualization of path-integrated fluid flow structures, such as shock waves, in the proposed flow paths. In this study, a z-type schlieren setup shown in Figure 3 was used due to the physical space constraints in the facility. Two 60 inch spherical mirrors were used to collimate the light. This allowed for the density refractive index gradients in the collimated light path region to be imaged by a Photron FastCam SA-Z high-speed camera operating at a frequency of 30 kHz. A repeatable release mechanism was employed for the entirety of the test campaign to release the 25.4 mm diameter spheres in free-flight configuration. The mechanism was made from a 3D printed flap mounted to a hinge, which then collapsed into a cavity after contact with the normal shock during startup flow of the tunnel, releasing the test article.

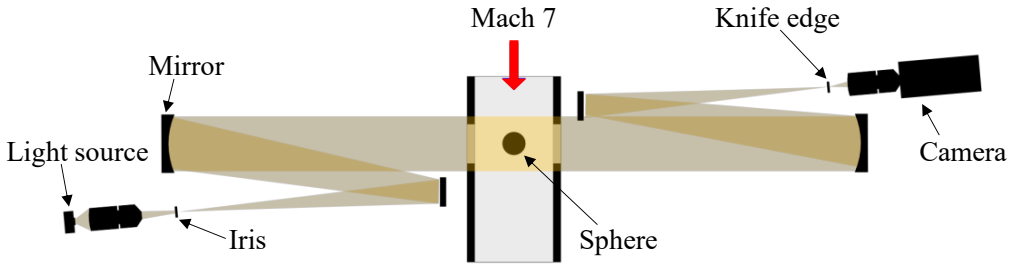

Figure 3: Z-type schlieren setup top view.

In this work, a total of four schlieren tests were performed to visualize the wake structures behind the models at Mach 7.2. Table 1 provides the facility's flow conditions for the schlieren tests on the strut-mounted and free-flight spheres. In all the images present in this study, flow is depicted from left to right.

Table 1: Facility operating conditions for schlieren.

Wind Tunnel Test	Model	Burst Pressure [MPa]	P_0 [MPa]	P [kPa]	Re $[\times 10^6\, m^{-1}]$	Re_d $[\times 10^4]$	Acquisition rate [kHz]
1	Strut-mounted	1.95	1.76	0.29	10.68	54.26	30
2	Free-flight	1.73	1.55	0.47	17.02	43.23	30
3	Free-flight	1.84	1.65	0.51	18.32	46.54	30
4	Free-flight	2.01	1.81	0.57	20.46	51.97	30

2. Molecular Tagging Velocimetry

In the acetone molecular tagging velocimetry non-intrusive laser technique, the 4th harmonic of a Spectral Energies QuasiModo Nd:YAG pulse-burst laser was operated at 10 kHz with a 10 ms burst mode, resulting in 100 pulses and ~80 mJ/pulse. Acetone gas was used as the seeded tracer molecule in air owing to acetone's broadband UV wavelength absorbance of light between 220 nm – 320 nm [33]. A similar seeding method described in the work by Andrade et al. was used in this study to seed the flow with acetone as the tracer gas [27]. The incident laser beam was guided through the ceiling of the test section using three 266 nm wavelength mirrors. Two 25.4 mm diameter focusing lenses with a 100 mm and a 150 mm focal point were used for the strut-mounted and the free-flight model, respectively. To capture the signal, a Photron FastCam SA-Z high speed camera coupled with a LaVision high-speed intensifier, and a AF Micro Nikkor 60 mm f/2.8 lens was used. The camera operated at 10 kHz with an exposure time of 40 µs, while the intensifier had an exposure time of 1µs. Figure 4 demonstrates the timing sequence of the laser, camera, and intensifier for a single pulse for test #1 in Table 2 where Δt is the time delay from the initial tagged line and varied between all of the runs in this test campaign. The 266 nm laser beam was filtered out by placing a Schott N-WG 295 glass filter in front of the camera lens.

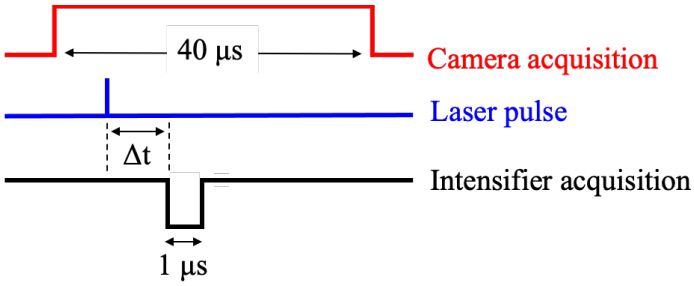

Figure 4: Timing Sequence.

Figure 5 demonstrates the MTV experimental setup for the strut-mounted stainless-steel model. For the strut-mounted setup, a pressure increase in the plenum initiates an output signal to trigger the laser, high-speed camera, and intensifier. The signal was delayed by 40 ms, to ensure the laser and imaging system initiate during the first steady-state pass. The incident beam was roughly 47.5 mm (0.94 $\frac{x}{d}$) from the center of the sphere.

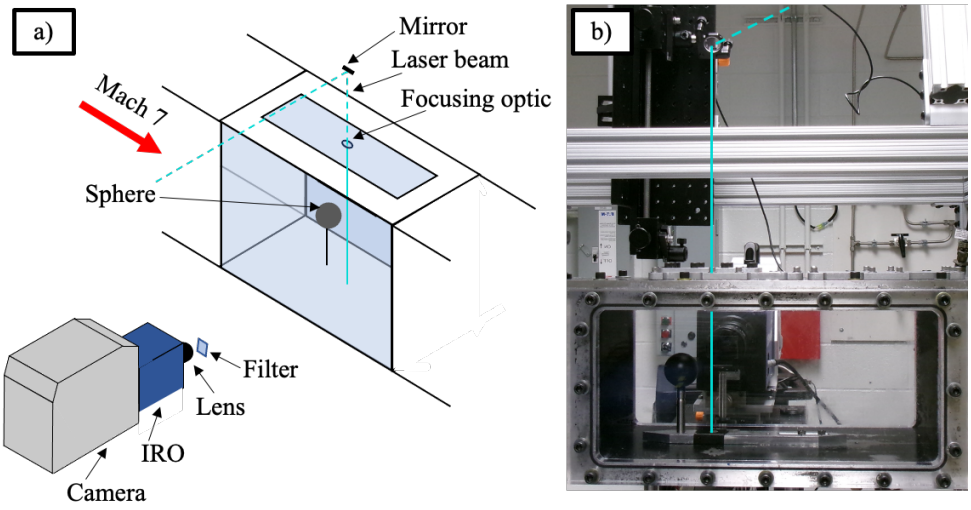

Figure 5: MTV experimental setup: strut-mounted model.

The MTV setup for the free-flight model is shown in Figure 6a. A 532 nm continuous laser was implemented in the spanwise direction in the free-flight system, where four lines, slightly less than 25.4 mm apart, were created by reflecting the incident beam as seen in Figure 6b. The end of the fourth 532 nm line was placed on a photodetector sensor to detect when the free-flight model crossed the beam path. This beam-break system provided a signal to trigger the laser, camera, and intensifier as opposed to the pressure transducer and there was no signal delay applied to the system. The 266 nm incident beam was 50.8 mm from the 532 nm continuous laser. The free-flight release mechanism used for MTV was the same one that was used for schlieren.

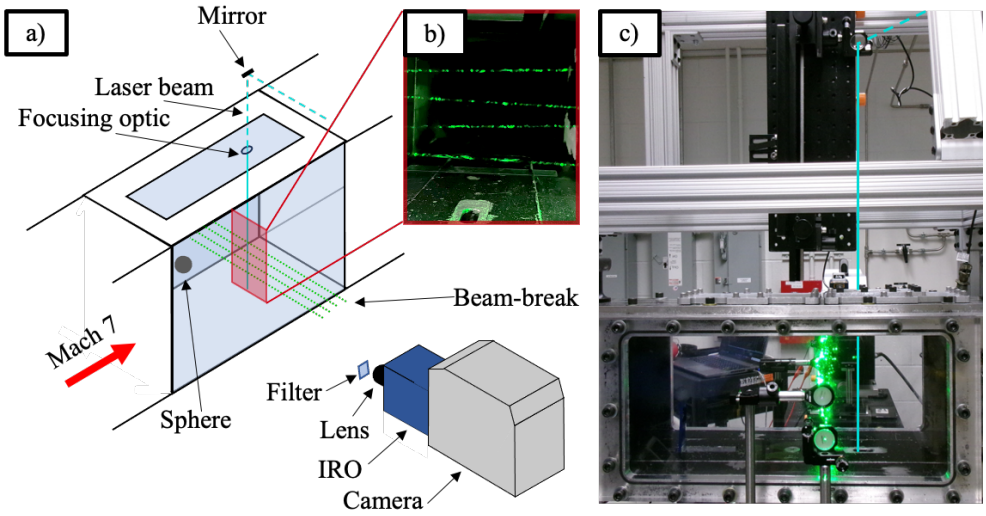

Figure 6: MTV experimental setup: free-flight model.

Quantitative off-body velocity measurements were performed on four strut-mounted cases and one free-flight case using MTV. Table 2 presents the flow conditions for each test case along with other experimental settings.

Table 2: Facility operating conditions for MTV.

Wind Tunnel Test	Model	Burst Pressure [MPa]	P_0 [MPa]	P [kPa]	Re [$\times 10^6\ m^{-1}$]	Acquisition rate [kHz]	Δt (ns)	Average Uncertainty (m/s)
1	Strut-mounted	1.66	1.49	0.45	16.21	10	650	± 11
2	Strut-mounted	1.77	1.59	0.41	14.63	10	1730	± 27
3	Strut-mounted	1.80	1.62	0.45	16.23	10	2230	± 30
4	Strut-mounted	1.68	1.51	0.40	14.55	10	2730	± 13
5	Free-flight	1.76	1.59	0.32	11.64	10	1000	± 66

IV. Numerical Program

A. Initial and Boundary Conditions

Initial and boundary conditions were known prior to the simulations for comparisons to each wind tunnel test. Beginning with the average freestream velocity reported by Andrade et al. and the Mach number of the wind tunnel facility used in this study, a freestream temperature was approximated using Equation 1 to obtain a freestream density based on known static pressure readings recorded by the facility's acquisition system [27,28]. Then, Sutherland's law shown in Equation 2 determined the freestream viscosity, assuming air as the working fluid. Reynolds number was also computed after freestream conditions were found. The initial and boundary conditions used to simulate the flow features are listed in **Error! Reference source not found.**.

$$M_\infty = \frac{u_\infty}{a_\infty} = \frac{u_\infty}{\sqrt{\gamma R T_\infty}} \tag{1}$$

$$\mu_\infty = \mu_0 \left(\frac{T_\infty}{T_0}\right)^{\frac{3}{2}} \left(\frac{T_0 + C}{T_\infty + C}\right) \tag{2}$$

Table 3: Facility conditions for simulation.

Model	M_∞	u_∞ [m/s]	T_∞ [K]	P [kPa]	ρ_∞[× 10^{-2} kg/m^3]	μ_∞ [× 10^{-6} kg/m*s]	Re [× $10^6\ m^{-1}$]	Re_d [× 10^4]
Free-flight	7.2	886	37.7	0.57	5.26	2.3	20.4	51.9

B. Flow Solver

The CFD approach used for this validation study is based on a continuous Galerkin spatial discretization with a Singly Diagonal Implicit Runge-Kutta (SDIRK) [35] two stage second order time stepping scheme. This numerical approach has shown well validated results for these types of flow fields in past studies [34-44]. The CFD solver used the Trilinos collection of packages [45-48]. Linear P1 tetrahedrons with a 2nd order Gaussian quadrature numerical integration scheme were used to discretize the domain. Implicit time integration used the SDIRK 2 stage 2nd order scheme with a slowly increasing global time step that was kept below a global Courant-Friedrichs-Lewy number of 10. Per stage of the SDIRK scheme a strict Newton solver was used drive the two-norm of the non-linear residual down three orders of magnitude. Per Newton step the resulting linear system was converged 5 orders of magnitude with a preconditioned Generalized Minimum Residual (GMRES) scheme accelerated by the Pardiso preconditioner [49,50]. The ParMetis KWAY spatial subdomain partitioning scheme was shown to appropriately spatially subdivide the mesh in such a way that the local linear systems were well conditioned and global linear convergence was obtained with minimal linear solver computational cost [51].

C. Grid Topology

To reduce manual meshing effort and maximize computational efficiency, an automated error driven anisotropic Adaptive Mesh Refinement (AMR) process was used to efficiently reduce spatial discretization error with minimal CFD analyst interaction. For example, a slice of the final adapted mesh is shown in Figure 7 and the corresponding grid size is the last row in Table 4. To automate the process, the pyCAPS framework from Engineering Sketch Pad was used to manage the AMR cycle [52]. PyCAPS seamlessly connects the adaptive mesher output to the solver inputs as well as the conformity of the surface mesh through the use of constructive solid modeling (CSM). The CSM file provided to pyCAPS consisted of a sphere of radius 0.0127 m positioned in a rectangular farfield where -X, ±Y, and ±Z boundaries were constricted to 50 radii from the sphere. The +X boundary was positioned 75 radii behind the sphere to allow for the fluid structures in the wake to develop. The farfield was set to a Riemann invariant boundary condition [53]. The sphere surface was an isothermal, no-slip wall with a wall temperature of 385 K.

With respect to the CFD problem statement, the AMR process was initiated with an initial grid generated with AFLR 3 & 4. NASA's Refine tool was used to adapt the new grids from an internally computed error field based on the scalar Mach number field generated from the CFD solver [54-58]. The adaptation schedule for the AMR process is shown in Table 4. Refine uses a metric referred to as 'complexity' for managing the number of points distributed throughout the adapted field [55]. Between each increase in complexity, 3 adaptation iterations were performed giving Refine opportunity to improve point distribution with a constant complexity target. Simply put, the complexity value will drive Refine to create roughly double that number of points. An adaptation iteration consists of both a solution from the flow solver and Refine producing a mesh adapted to that generated solution. The adaptation schedule below was created in two phases. The first phase started with a complexity value of 50,000 and was increased by 20% after the 3 adaptation iterations mentioned earlier. This growth rate was applied 13 times to a complexity of 445.8 thousand at which point the startup transients had passed and the solution had reached steady state. The final 6 complexity iterations started with a complexity value of 600 thousand and with a growth rate of 1.5. Table 4 shows the full history of the grid size through the AMR process.

Table 4: Complexity Schedule and Grid Specifics.

	Initial Complexity (thousand)	Vertices	Tetrahedra
Phase 1	AFLR	34,951	204,567
	50	102,191	590,349
	60	121,276	695,988

	72	146,463	838,006
	86.4	177,733	1,006,803
	103.6	209,577	1,208,771
	124.4	251,401	1,457,839
	149.3	300,652	1,744,878
	179.2	360,353	2,089,147
	215	430,434	2,485,199
	258	515,980	2,980,414
	309.6	616,226	3,589,259
	371.5	745,447	4,289,398
	445.8	887,023	5,155,746
Phase 2	600	1,159,448	6,717,898
	900	1,751,351	10,158,543
	1350	2,682,678	15,615,313
	2025	4,000,032	23,313,764
	3037.5	5,982,225	34,892,222
	4556.3	8,953,897	52,375,475

The initial grid is shown in the first row of Figure 7 AFLR produces a traditional extruded grid where the boundary layer follows a regular growth pattern after which it smoothly transitions to the farfield region. The 50k complexity grid in Figure 7 shows how Refine has adapted to the error field from the initial solution on the original AFLR grid. The Mach number distribution shows that the computational grid is resolved enough such that the bow shock and lip shock are forming in the computed solution. However, the error field in the 50k row of Figure 7 how the flow structures have not been able to form in the wake region. The 180k complexity grid at the bottom of Figure 7 can support the formation of the recirculation region as well as the recompression shock. Evidence of the complexity growth rate sharply increasing can be seen in the wide view of the 600k mesh. However as shown in the bottom row of Figure 7 by the time the complexity has grown to 4 million the mesh resolution has allowed more flow structures to be resolved. Furthermore, Refine has efficiently adapted as wide-angle view of the mesh does not show similar overcrowding in the isotropic region. The solution was deemed fully mature at a complexity of 4 million as all the flow structures noted in the Figure 9 had formed and the transients in the wake region appeared to be fully resolved.

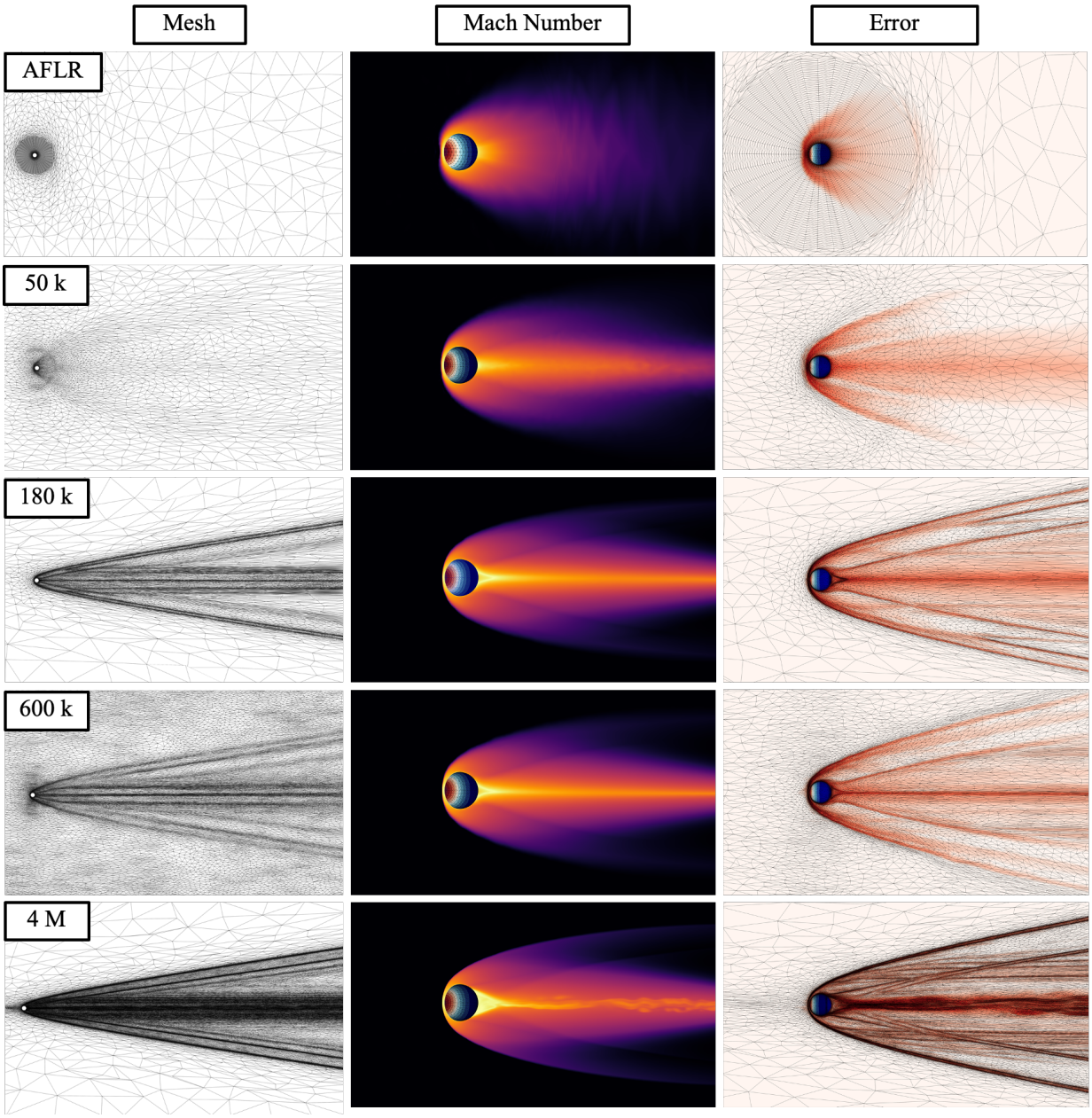

Figure 7: Grid topologies (complexity value), Mach number, and dominant error fields of various complexities in the AMR process.

V. Results and Discussion

A. Schlieren Imaging

For the schlieren results presented in this study, an in-house Python code was used to process the run images. The images were first realigned by using a sub-pixel phase-base cross-correlation function owing to the facility's slight recoil during the rupture of the diaphragm. Then, the code consisted of dividing the wind-on images by an average wind-off image taken prior to the test to remove any background noise present in the path integrated collimated light. Only images in the first steady-state pass were used and processed for the strut-mounted model. Figure 8 demonstrates a time-averaged schlieren image, calling out the wake structures observed. The fluid structures that are seen generated by the sphere include the bow shock, lip shock, and shear layer. It can be seen that as the boundary layer begins to separate from the sphere, a viscous shear layer with recirculating flow begins to form in the near wake region. Based

on previous literature, the recirculating region in the viscous shear layer is known to have high temperature and pressure gradients and low density gradients [1,10].

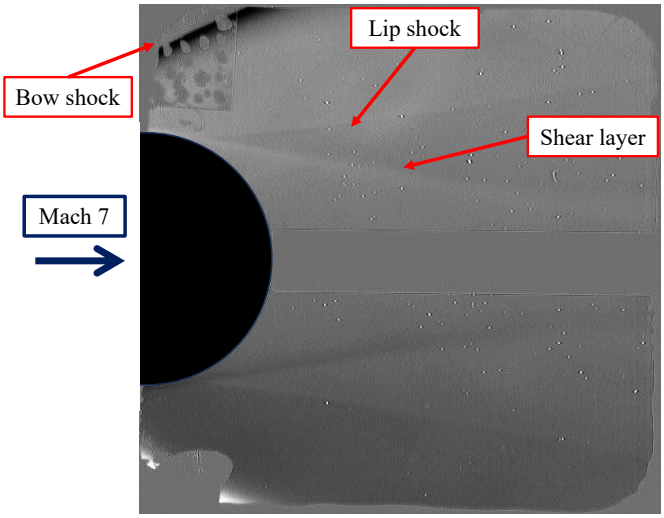

Figure 8: Time-averaged schlieren of strut-mounted sphere.

As discussed, schlieren imaging was also implemented on the free-flight spheres with a smaller diameter, and a similar z-type schlieren configuration was used for the spheres. A time-averaged schlieren image is shown in Figure 9. Similar wake structures in the near wake observed in the strut-mounted case were also seen in the near wake of the free-flight case. Important fluid flow features that were witnessed in the far wake of the free-flight model were the recompression shocks. As the fluid begins to transition from the near wake to the far wake, a second stagnation point occurs in the wake neck where the flow velocity decreases, and the flow temperature increases [16]. Then, recompression shocks emanate from the stagnation point located in the wake neck and turbulent structures in the inner wake are known to develop between the two recompression shocks after the wake neck [1].

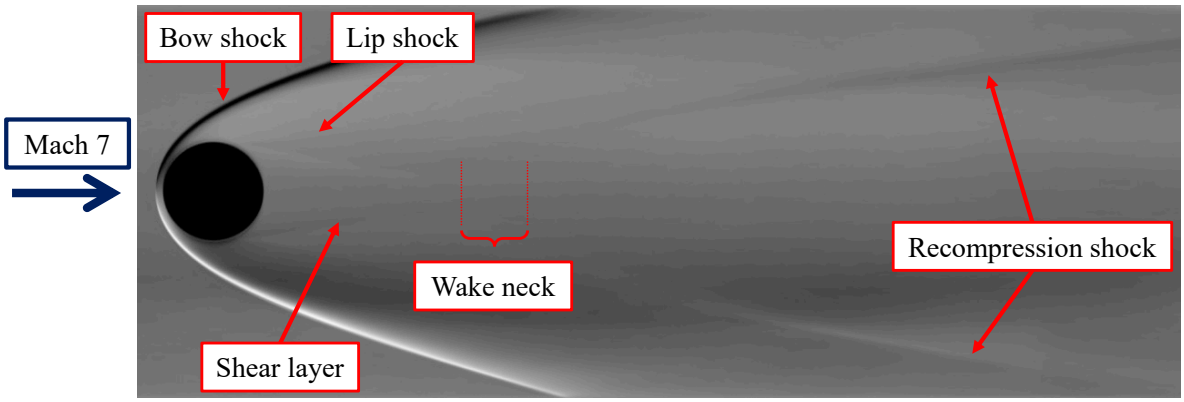

Figure 9: Time-averaged schlieren image with wake structures labeled.

B. Molecular Tagging Velocimetry

An initial write line was recorded subsequently from the end of the delayed line for each test listed in Table 2. For the results presented in this study, the same processing method was used for all cases. The processing method is similar to the method described in the work done by Andrade et. al and was applied to the first half of the images for every wind tunnel test [27]. Figure 10 demonstrates a diagram of the processing method used. Turbulent fluctuations were observed in the wind-on strut-mounted MTV images, and the delayed image in Figure 10 shows a single image in the wind-on dataset. The delayed images were pre-processed using ImageJ by applying a median filter with a radius of 70, on an averaged wind-on image and subtracting it from the first half of the wind-on images. As the delay time increased, the signal intensity began to decrease due to the decay of the acetone's fluorescence. To mitigate the signal-to-noise (SNR) ratio, a threshold finding filtering method was used to remove any outliers outside of the MTV signal

that were present in the images. Then, a gaussian fit was applied to every row for every image in the dataset to find the signal peak and any points outside the bounds of ±2σ were removed. Figure 10 shows test #1 from Table 2 with the overlay of the peaks found in red and their respective MTV lines. Once the peaks were obtained, every five rows were averaged for the initial and delayed image and the pixel shift between the write and delayed line was found. From the pixel shift, and the given time delay, velocity profiles were calculated.

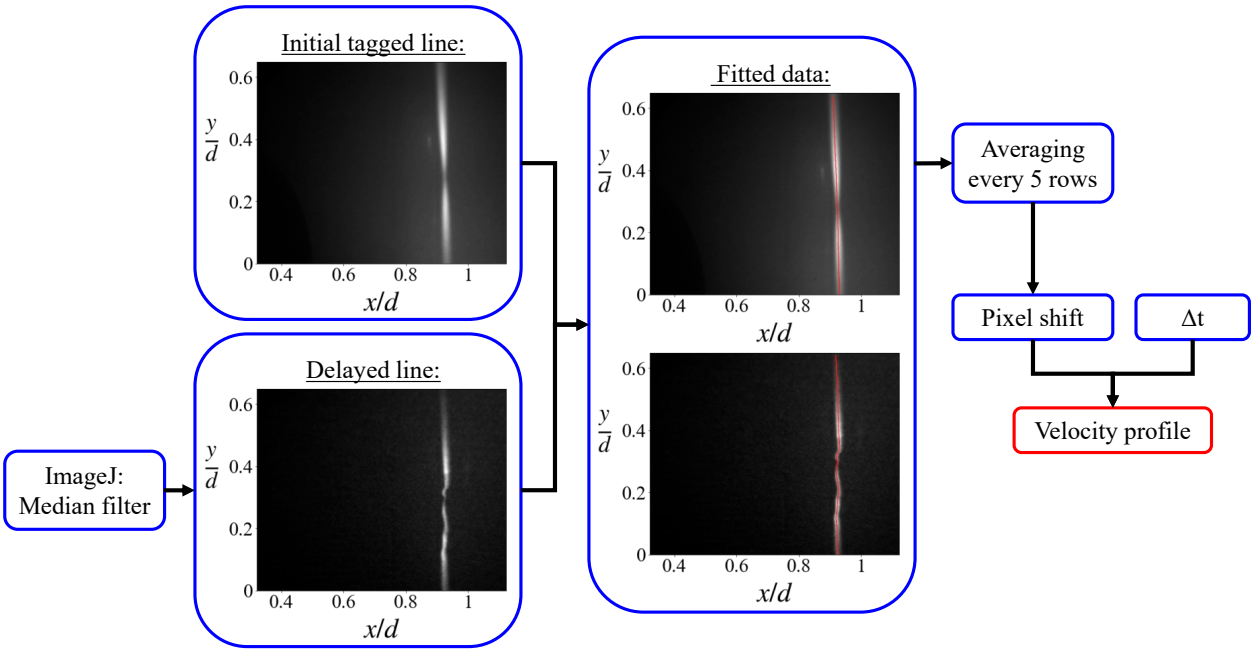

Figure 10: Data processing method.

The velocity profiles for every image were then time-averaged to obtain an averaged velocity profile shown in Figure 11, along with a turbulent root mean square (RMS) profile to demonstrate the turbulent fluctuations observed on the strut-mounted cases using MTV. According to Lykoudis, turbulence in the shear layer occurs due to high vorticity that is present in that region [4].

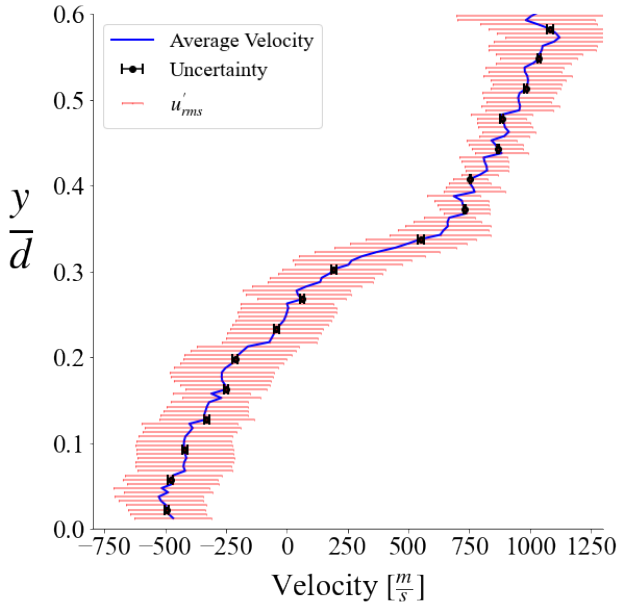

Figure 11: Strut-mounted test#1 velocity profile.

To estimate the uncertainty of the velocity profiles, a Student's t-distribution was executed where the margin of error in Equation 3 is represented by the uncertainty on the mean velocity profile, *n* is the number of frames in the dataset per test, σ is the standard deviation based on the turbulent fluctuations, and *t* is the critical value corresponding to a 95% confidence level and the degrees of freedom (i.e. *n*-1). This approach led to an average uncertainty value listed in Table 2 for each wind tunnel test. Figure 12 demonstrates the RMS velocity for test #1, where the minimum RMS value seen is 11.5 m/s and the maximum is 48 m/s.

$$Margin\ of\ error = t * \frac{\sigma}{\sqrt{n}} \tag{3}$$

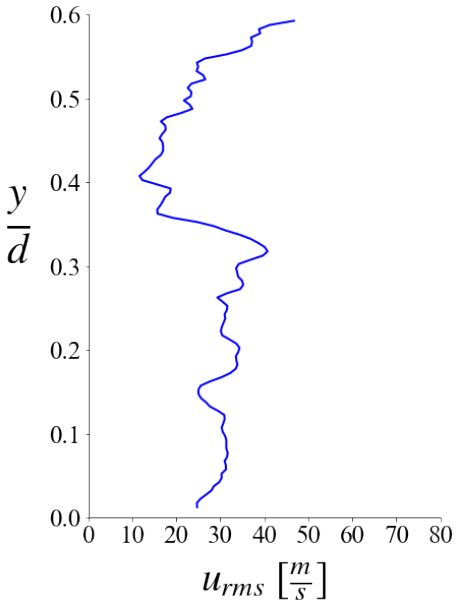

Figure 12: RMS of velocity.

From Figure 11, reversed flow, denoted by negative velocity values, were present inside the viscous shear layer, where the flow is known to be recirculating by previous literature [12,59,60]. In the study completed by Hruschka et al., velocity values of up to -500 m/s were observed in the shear layer of the Mars Microprobe using nitric oxide PLIF and direct simulation Monte Carlo (DSMC) under Mach 9.7 flow conditions [20]. Similarly, negative velocities in the shear layer have also been seen under supersonic Mach 2.5 flow conditions of a circular cylinder by Herrin and Dutton [16]. And detached eddy simulations computed by Brock et.al similarly witnessed negative streamwise velocity values in the recirculation region of the Orion Exploration Vehicle [61]. All four strut-mounted cases with different time delays are plotted in Figure 13 along with their respective uncertainties.

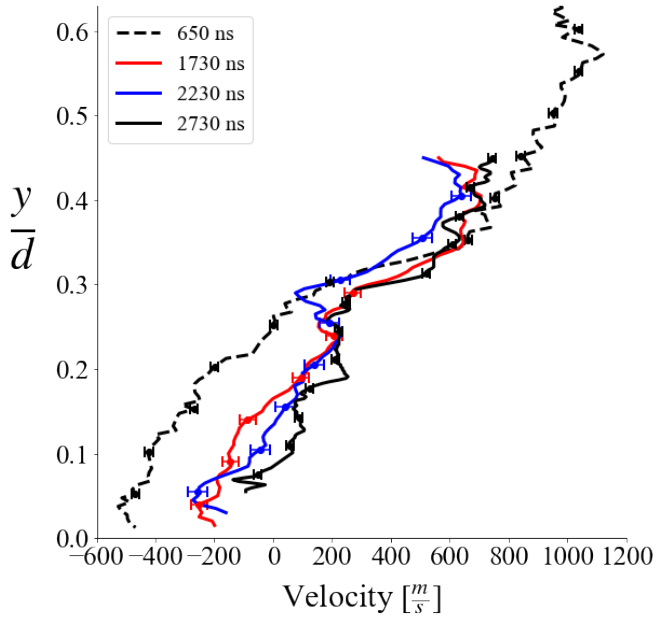

Figure 13:Velocity profile for all strut-mounted cases.

To obtain a velocity scan of the shear layer, MTV was performed on the 25.4 mm diameter sphere in free-flight. To the author's knowledge, this is the first time any non-intrusive laser diagnostic has been performed on a free-flight model in hypersonic flow. Since the model was in free-flight, each frame in the dataset contributed to a velocity profile at different locations in the near wake of the sphere. Consequently, a Student's t approach was not implemented but rather an uncertainty propagation approach was used based on Δt of 1 μs between the intensifier exposure and a laser pulse, a 6 ns manufacturer reported time uncertainty for the intensifier, and a ± 2 pixel tracking accuracy of both the delayed and initial write line. This resulted in an average uncertainty of ± 66 m/s for the free-flight case. Similar to the strut-mounted case, the free-flight case experienced negative velocity throughout the recirculation region in the shear layer as shown in Figure 14. An overlay of the schlieren image with the fluid structures labeled and the velocity profile contour in the viscous shear layer is depicted in Figure 15. A comparison of the strut-mounted velocity profiles to the free-flight velocity profiles at the same location, denoted by the white dashed line in Figure 15, is shown in Figure 16 at roughly 0.94 $\frac{x}{d}$. Overall, both the strut-mounted and free-flight case showed similar negative velocities in the shear layer in the near wake of the sphere.

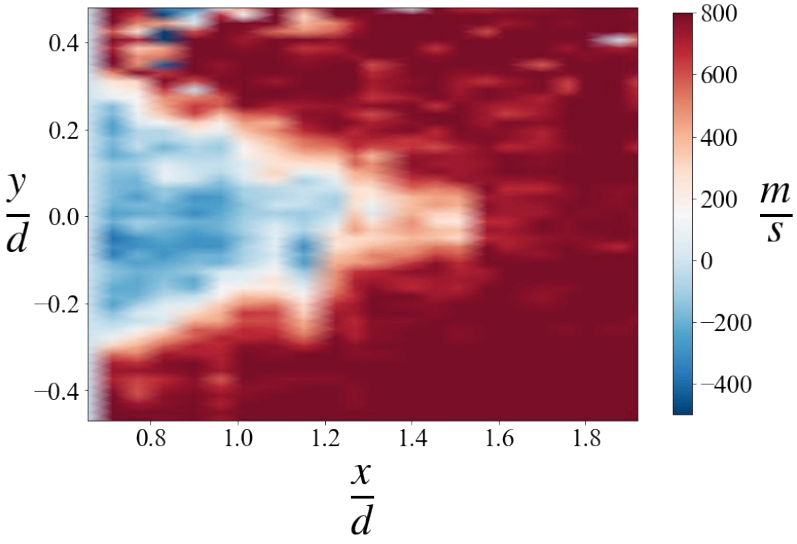

Figure 14: Free-flight velocity contour.

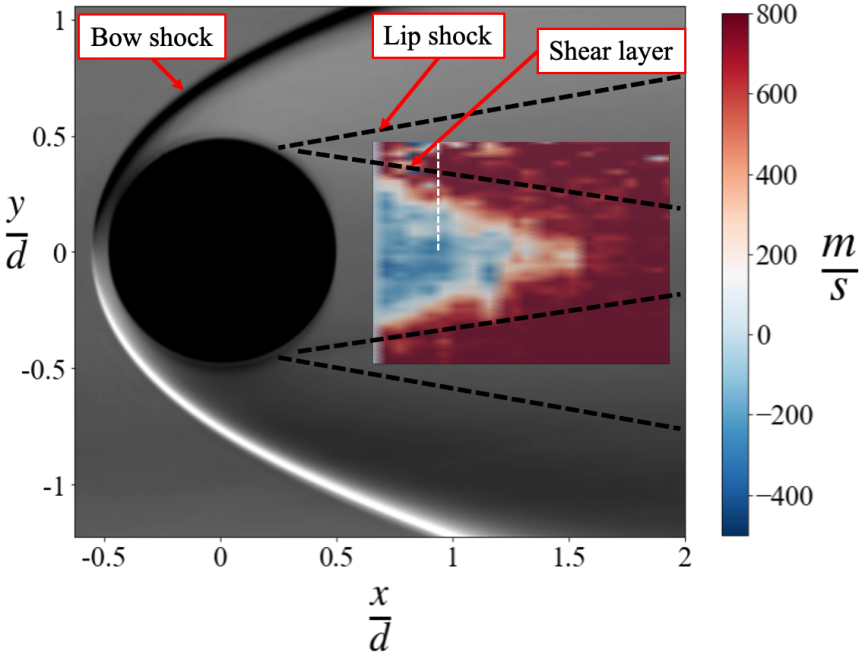

Figure 15: Free-flight schlieren overlay with velocity contour.

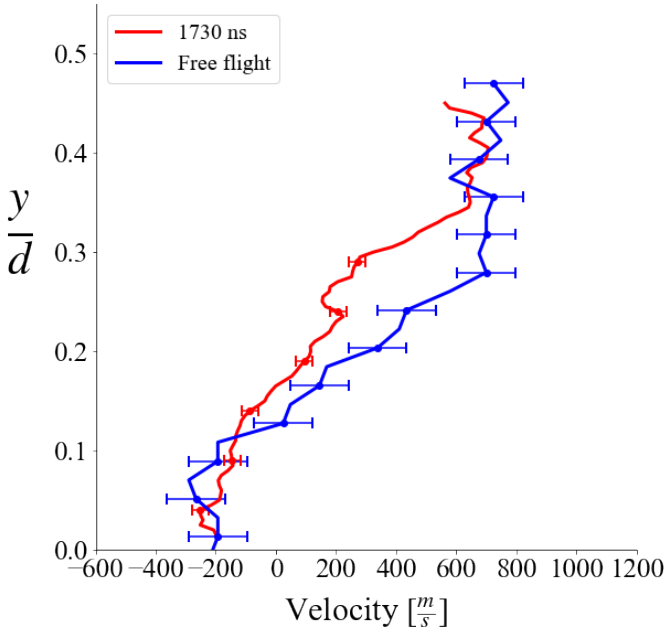

Figure 16: Velocity profile comparison of strut-mounted case vs free-flight case.

C. Computational Fluid Dynamics

The experimental results were used to validate the above stated CFD solution and mesh adaptation process. Specifically, the validation was carried out by comparing the CFD fluid structures present in the center plane schlieren to experimental schlieren images. Also, CFD streamwise velocity profiles were compared to experimental MTV velocities. A comparison of the experimental and computational schlieren is depicted in Figure 17 where the experimental is shown on the bottom half while the simulated results are shown on the top half of the image. The CFD computed bow shock, lip shock, shear layer, and recompression shock features show good agreement with their counterparts in the experimental schlieren.

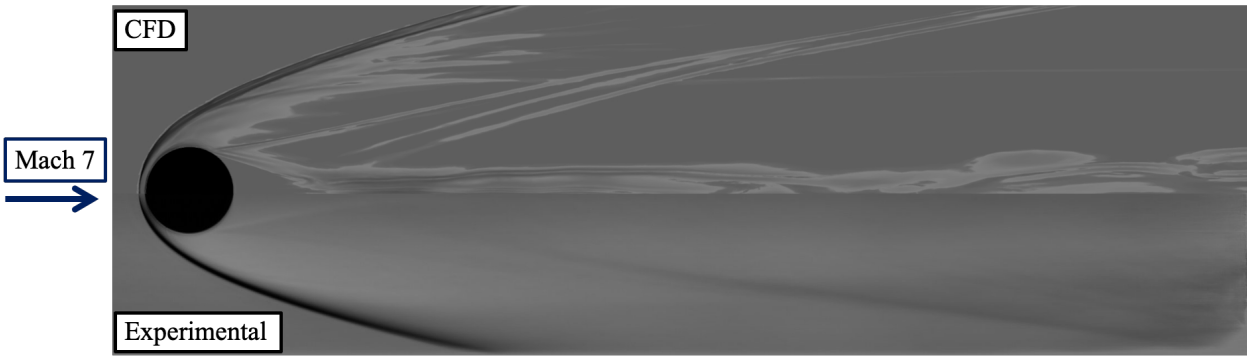

Figure 17: Schlieren comparison of experimental vs CFD.

Figure 18a and Figure 18b show the simulated results of the wake region. The synthetic schlieren in Figure 18a shows how the bow shock and recompression shock propagate to the farfield with minimal dissipation. Figure 18b shows the mesh at the end of the adaptation process. Interesting flow vortices developed in the inner wake after the wake neck in the simulated results. A total of four vortex-like structures are seen in a clover-like form in Figure 19. Further experimental work will need to be done in order to verify these quad vortex-like flow features seen in the far wake.

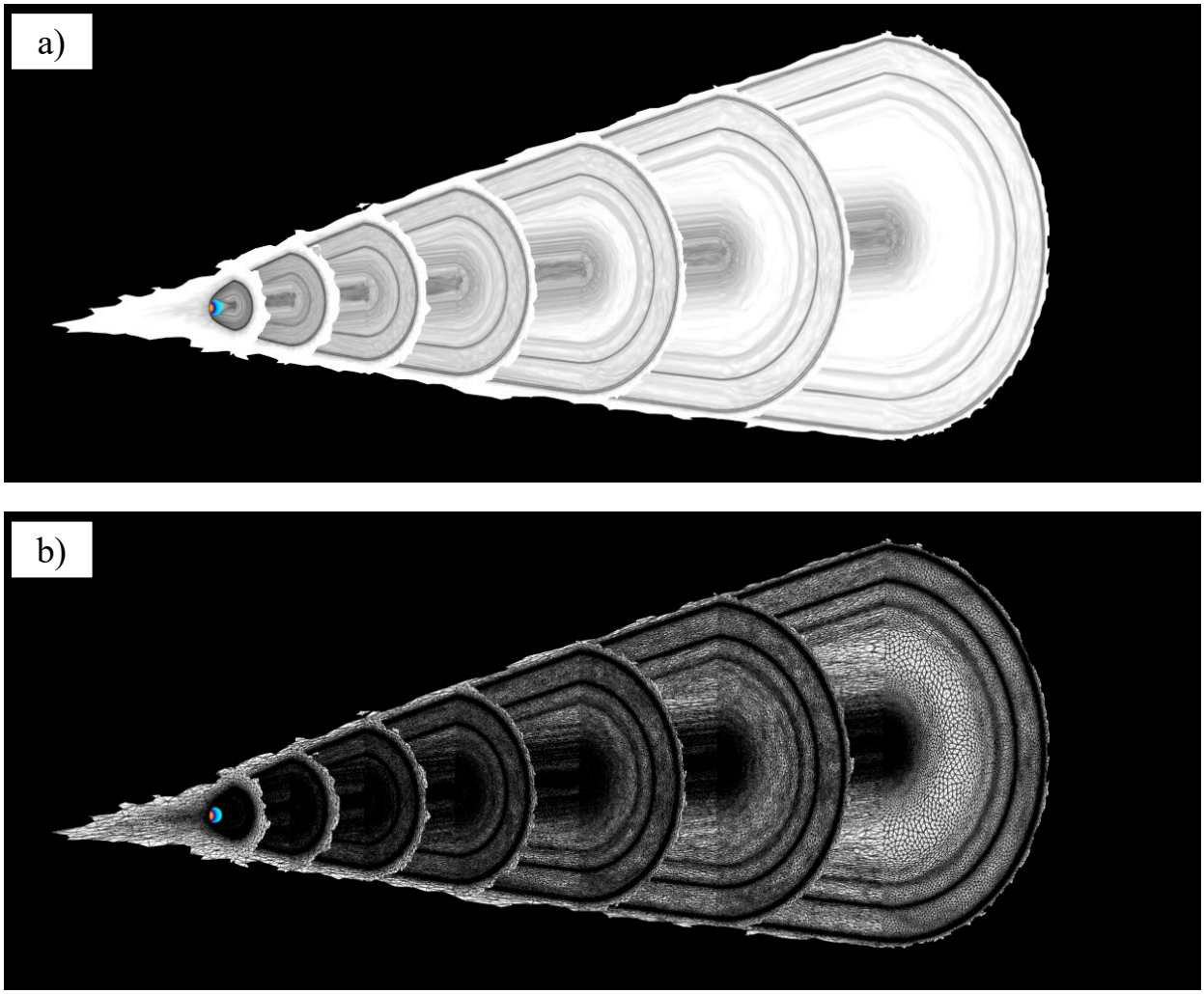

Figure 18: a) synthetic schlieren of the wake region, b) grid topology of the wake region.

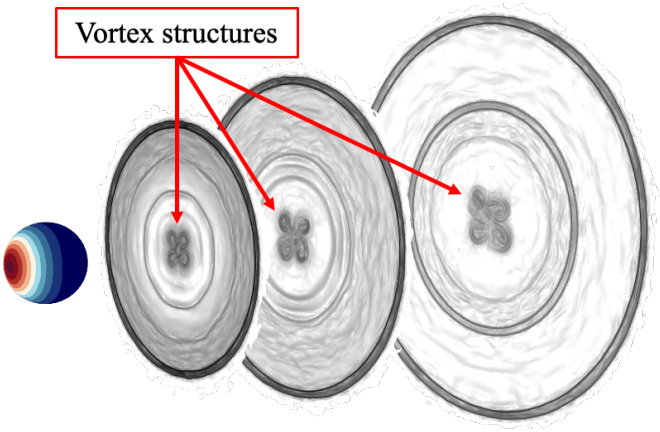

Figure 19: Quad vortex-like structures in the inner wake.

From the free-flight case, the experimental velocity contour was compared to a simulated velocity contour at the same location in the near wake of the sphere and is demonstrated in Figure 20. In both the CFD and experimental results, reverse flow with negative velocities was witnessed in the recirculation region in the viscous shear layer. The recirculation region in the simulated results also shows to be in good agreement with the starting location of $\frac{y}{d}$ as in the experimental results. A velocity line profile was taken at 0.94 $\frac{x}{d}$ for both in the experimental and CFD and is shown in Figure 21. The CFD results showed to be in the bounds of uncertainty of the experimental results, although at 0.1 $\frac{y}{d}$, the experimental data presented lower velocities than the CFD data. This phenomenon was also observed in the work conducted by Hruschka et al. [20]. To conclude the findings in this study, Figure 22 shows an overlay of the CFD and experimental velocity contours on the schlieren with the flow structures of the wake labeled.

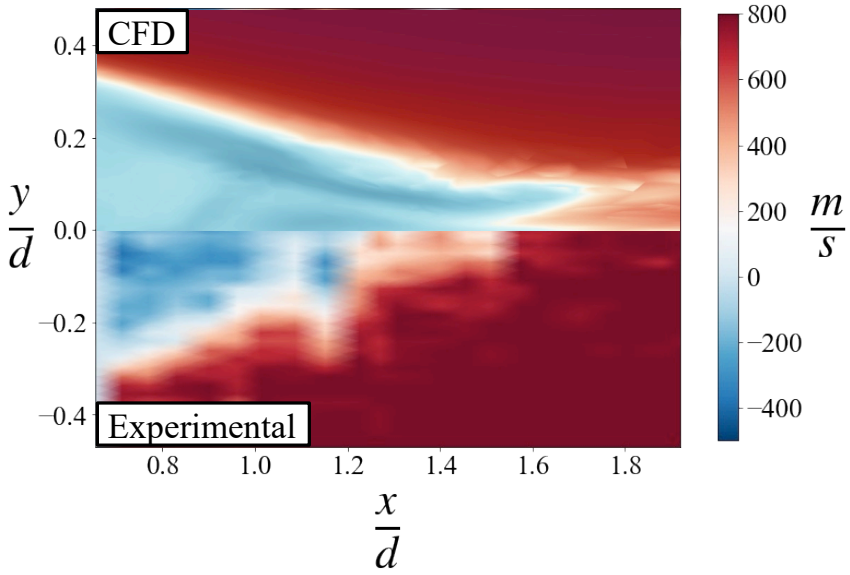

Figure 20: Velocity contour of experimental vs CFD.

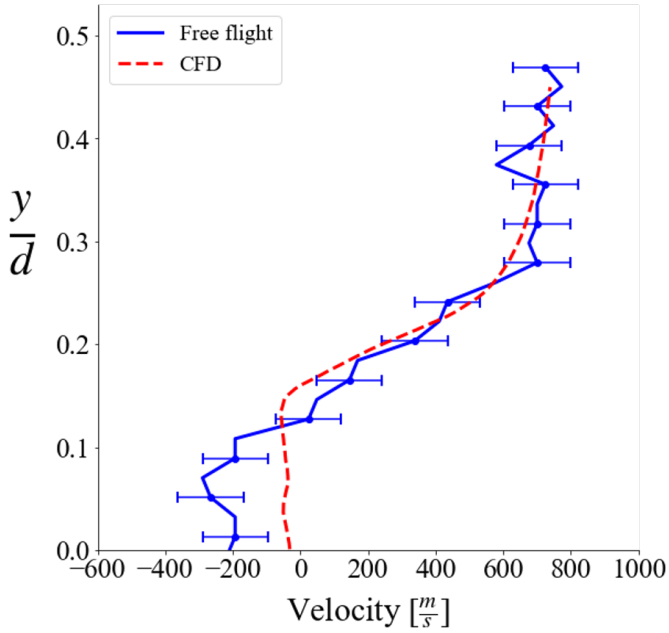

Figure 21: Velocity line profile at 0.94 $\frac{x}{d}$.

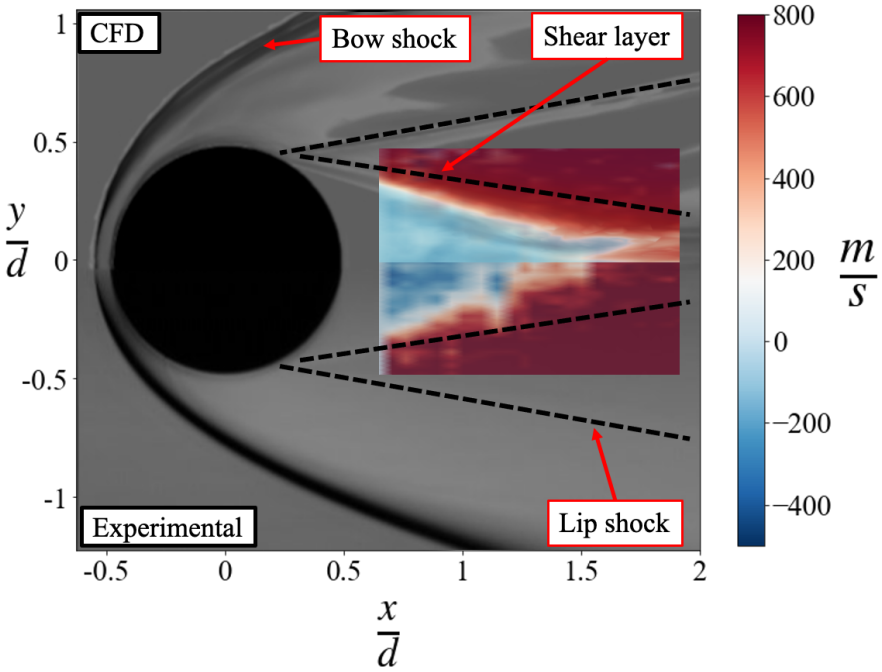

Figure 22: Overlay of experimental and CFD velocity contours on schlieren.

VI. Conclusion

The schlieren results with the strut-mounted and free-flight sphere test cases capture the fluid structures in the wake region of a sphere, including the recirculation region and shear layer in the near wake and the wake neck and recompression shocks further downstream. Quantitative velocity measurements were taken with acetone molecular tagging velocimetry and showed large velocity values in the reversed flow in the recirculation region, which are consistent with the existing literature. This non-intrusive technique demonstrated an approach to collect velocity information without distorting the wake behind a sphere and having a minimal impact on the fluid flow. To the authors

knowledge, this study also showed the first use of laser diagnostics to collect off-body velocity measurements of a representative body in free-flight under hypersonic conditions. The computational fluid dynamics results agree with the experimental results and additionally show how far downstream the bow shock and recompression shocks influence the wake turbulence without dissipating. The AMR and low dissipation techniques used help to validate the techniques on a simple geometry. This also shows a strong vorticity content traveling far downstream of the sphere.

Future work will apply the same laser diagnostic technique to obtain velocity measurements in the far wake and will look at more non-intrusive techniques to study the temperatures, pressures, and species content of the wake. Additional refinement of computational models will continue to inform these measurements and will be the focus of ongoing investigations. Together, these joint studies will inform a more comprehensive understanding of how the turbulent structures in the recompression region develop.

Acknowledgments

This research was supported by Oak Ridge National Laboratory under award number DE-AC05-00OR22725. The views and conclusions contained herein are those of the authors and should not be interpreted as necessarily representing the official policies or endorsements, either expressed or implied, of Oak Ridge National Laboratory or the U.S. Government. The authors would also like to thank Patrick Hughes and Rafael Lopez from the Hypersonics Lab at UTSA for their help in this study.

References

[1] Lees, L. "Hypersonic wakes and trails," *AIAA Journal* Vol. 2, No. 3, 1964, pp. 417-428.
[2] Levensteins, Z. J., and Krumins, M. V. "Aerodynamic characteristics of hypersonic wakes," *AIAA Journal* Vol. 5, No. 9, 1967, pp. 1596-1602
[3] Levensteins, Z.J, and Krumins, M.V. "Experimental study of aerodynamic characteristics of hypersonic wakes," *3rd and 4th Aerospace Sciences Meeting* 1966-53
[4] Lykoudis, P. S. "A review of hypersonic wake studies," *AIAA Journal* Vol. 4, No. 4, 1966, pp. 577-590
[5] Bailey, A., and TN, A. E. D. C. A. A. "Observations of Sphere Wakes Over a Wide Range of Velocities and Ambient Pressures," *Rept. AEDC-TR-68-112*, 1968
[6] Fay, J. A., and Goldburg, A. "Unsteady Hypersonic Wake Behind Blunt Bodies," *AIAA Journal* Vol. 1, No. 10, 1963, pp. 2264-2272.
[7] R. Wilson, "Aerodynamic interference of pitot tubes in a turbulent boundary layer at supersonic speed," AIAA Journal 11, 1420-1421 (1973).
[8] Horvath, T., McGinley, C., and Hannemann, K.,"Blunt body near-wake flow field at Mach 6," *Fluid Dynamics Conference* 1996-1935.
[9] Lysenko, V. I. "Experimental studies of stability and transition in high-speed wakes," *Journal of Fluid Mechanics* Vol. 392, 1999, pp. 1-26
[10] Todisco, A., and Pallone, A. J. "Near wake flow field measurements," *AIAA Journal* Vol. 3, No. 11, 1965, pp. 2075-2080.
[11] Behrens, W. "The far wake behind cylinders at hypersonic speeds. I," *AIAA Journal* Vol. 5, No. 12, 1967, pp. 2135-2141.
[12] Dewey, C. F. "Near wake of a blunt body at hypersonic speeds," *AIAA Journal* Vol. 3, No. 6, 1965, pp. 1001-1010.
[13] Murman, E. M. "Experimental studies of a laminar hypersonic cone wake," *AIAA Journal* Vol. 7, No. 9, 1969, pp. 1724-1730.
[14] Hama, F. R. "Experimental studies on the lip shock," *AIAA Journal* Vol. 6, No. 2, 1968, pp. 212-219.
[15] Zakkay, V., and Cresci, R. J. "An experimental investigation of the near wake of a slender cone at M infinity equal 8 and 12," *AIAA Journal* Vol. 4, No. 1, 1966, pp. 41-46.
[16] Herrin, J. L., and Dutton, J. C. "Supersonic base flow experiments in the near wake of a cylindrical afterbody," *AIAA Journal* Vol. 32, No. 1, 1994, pp. 77-83.
[17] Herrin, J., and Dutton, J. C. "Effect of a rapid expansion on the development of compressible free shear layers," *Physics of Fluids* Vol. 7, No. 1, 1995, pp. 159-171.
[18] Mills, J., Sukenik, C., and Balla, R.,"Hypersonic wake diagnostics using laser induced fluorescence techniques," *42nd AIAA Plasmadynamics and Lasers Conference in conjunction with the 18th International Conference on MHD Energy Conversion (ICMHD)* 2011-3459.
[19] Hruschka, R., O'Byrne, S., and Kleine, H. "Two-component Doppler-shift fluorescence velocimetry applied to a generic planetary entry probe model," *Experiments in Fluids* Vol. 48, No. 6, 2009, pp. 1109-1120.
[20] Hruschka, R., O'Byrne, S., and Kleine, H. "Comparison of velocity and temperature measurements with simulations in a hypersonic wake flow," *Experiments in Fluids* Vol. 51, No. 2, 2011, pp. 407-421.
[21] Lachney, E., and Clemens, N. "PLIF imaging of mean temperature and pressure in a supersonic bluff wake," *Experiments in Fluids* Vol. 24, No. 4, 1998, pp. 354-363.
[22] Combs, C. S., Clemens, N. T., Danehy, P. M., and Murman, S. M. "Heat-shield ablation visualized using naphthalene planar laser-induced fluorescence," *Journal of Spacecraft and Rockets* Vol. 54, No. 2, 2017, pp. 476-494.
[23] Humble, R., Scarano, F., and Van Oudheusden, B. "Unsteady flow organization of compressible planar base flows," *Physics of Fluids* Vol. 19, No. 7, 2007.
[24] Scarano, F., and Oudheusden, B. W. "Planar velocity measurements of a two-dimensional compressible wake," *Experiments in Fluids* Vol. 34, No. 3, 2003, pp. 430-441.
[25] Bathel, B. F., Danehy, P. M., Inman, J. A., Jones, S. B., Ivey, C. B., and Goyne, C. P. "Velocity profile measurements in hypersonic flows using sequentially imaged fluorescence-based molecular tagging," *AIAA journal* Vol. 49, No. 9, 2011, pp. 1883-1896.
[26] Zhang, Y., Richardson, D. R., Beresh, S. J., Casper, K. M., Soehnel, M., Henfling, J., and Spillers, R.,"Hypersonic wake measurements behind a slender cone using FLEET velocimetry," *AIAA aviation 2019 Forum* 2019-3381.

[27] Andrade, A., Hoffman, E. N., LaLonde, E. J., and Combs, C. S. "Velocity measurements in a hypersonic flow using acetone molecular tagging velocimetry," *Optics Express* Vol. 30, No. 23, 2022, pp. 42199-42213.
[28] Hoffman, E. N., LaLonde, E. J., Andrade, A., Chen, I., Bilbo, H. A., and Combs, C. S. "Flow Characterization of the UTSA Hypersonic Ludwieg Tube," *Aerospace* Vol. 10, No. 5, 2023, p. 463
[29] Behrens, Wilhelm, ``Far Wake behind Cylinders at Hypersonic Speeds. Part II: Stability,'' AIAA Journal, Vol. 6, No. 2, February 1968, pp. 225-232.
[30] Gnoffo, Peter, ``Planetary-Entry Gas Dynamics,'' *Annual Review of Fluid Mechanics*, Vol. 31, January 1999, pp. 459-494.
[31] Reis, Victor, "Chemiluminescent Radiation from the Far Wake of Hypersonic Spheres,'' *AIAA Journal*, Vol. 5, No. 11, November 1967, pp. 1928-1933.
[32] Taylor, R. L., B.W. Melcher II, and W. K. Washburn, ``Studies of the Luminous Hypersonic Wake,'' *AIAA Journal*, Vol. 2, No. 10, October 1964, pp. 1731-1738.
[33] Samouda, F., Barrot, C., Colin, S., Baldas, L., and Laurien, N.,"Analysis of gaseous flows in minichannels by molecular tagging velocimetry," *International Conference on Nanochannels, Microchannels, and Minichannels* 2012-221-228.
[34] Glasby, R. S., and Erwin, J. T,"Introduction to COFFE: the next-generation HPCMP CREATETM-AV CFD solver," *54th AIAA aerospace sciences meeting* 2016-0567.
[35] Holst, K. R., Glasby, R. S., and Bond, R. B. "On the effect of temporal error in high-order simulations of unsteady flows," *Journal of Computational Physics* Vol. 402, 2020, p. 108989
[36] Holst, K. R., Glasby, R. S., Erwin, J. T., Stefanski, D. L., and Bond, R. B.,"High-order time-accurate simulations using HPCMP CREATE (TM)-AV Kestrel component COFFE," *2018 AIAA Aerospace Sciences Meeting* 2018-0027.
[37] Michal, T., Babcock, D., Kamenetskiy, D., Krakos, J., Mani, M., Glasby, R., Erwin, T., and Stefanski, D. L. "Comparison of fixed and adaptive unstructured grid results for drag prediction workshop 6," *Journal of Aircraft* Vol. 55, No. 4, 2018, pp. 1420-1432
[38] Holst, K. R., Glasby, R. S., Erwin, J. T., Stefanski, D. L., Prosser, D., Anderson, W. K., and Wood, S. L.,"Current status of the COFFE solver within HPCMP CREATETM-AV Kestrel," *AIAA Scitech 2020 forum* 2020-1530
[39] Holst, K. R., Glasby, R. S., Erwin, J. T., Stefanski, D. L., Bond, R. B., and Schmisseur, J. D.,"High-order simulations of shock problems using HPCMP CREATE (TM)-AV Kestrel COFFE," *2018 AIAA Aerospace Sciences Meeting* 2018-1301
[40] Holst, K. R., Glasby, R. S., Erwin, J. T., Stefanski, D. L., and Bond, R. B.,"High-order large eddy simulation validation in HPCMP CREATE (TM)-AV kestrel component coffe," *2018 AIAA Aerospace Sciences Meeting* 2018-0781
[41] Galbraith, M. C., Ursachi, C.-I., Chandel, D., Allmaras, S. R., Darmofal, D. L., Glasby, R. S., Stefanski, D. L., Erwin, J. T., Holst, K. R., and Hereth, E.,"Comparisons of HPCMP CREATETM-AV Kestrel-COFFE, SU2, and MIT SANS RANS Solutions using Output-Based Adapted Meshes for a Multi-Element Airfoil," *AIAA Scitech 2021 Forum* 2021-1080
[42] Nutter, N. F., Cobourn, J. W., Bond, R. B., Kreth, P. A., Schmisseur, J. D., Glasby, R. S., Stefanski, D. L., Hereth, E., and Coder, J. G.,"Simulations of dynamic shock wave/boundary layer interactions using HPCMP CREATETM-AV Kestrel COFFE," *AIAA Scitech 2021 Forum* 2021-0499
[43] Holst, K. R., Glasby, R. S., Erwin, J. T., Stefanski, D. L., and Coder, J. G.,"High-Order Shock Capturing Techniques using HPCMP CREATE-AV Kestrel," *AIAA Scitech 2019 Forum* 2019-1345.
[44] Galbraith, M. C., Ursachi, C.-I., Chandel, D., Allmaras, S. R., Darmofal, D. L., Glasby, R. S., Stefanski, D. L., Taylor Erwin, J., Holst, K. R., and Hereth, E. A. "Comparing multi-element airfoil flow solutions using multiple solvers with output-based adapted meshes," *AIAA Journal* Vol. 60, No. 4, 2022, pp. 2629-2643
[45] Notz, P. K., Pawlowski, R. P., and Sutherland, J. C. "Graph-based software design for managing complexity and enabling concurrency in multiphysics PDE software," *ACM Transactions on Mathematical Software (TOMS)* Vol. 39, No. 1, 2012, pp. 1-21
[46] Pawlowski, R. P., Phipps, E. T., and Salinger, A. G. "Automating embedded analysis capabilities and managing software complexity in multiphysics simulation, Part I: Template-based generic programming," *Scientific Programming* Vol. 20, No. 2, 2012, pp. 197-219
[47] Pawlowski, R. P., Phipps, E. T., Salinger, A. G., Owen, S. J., Siefert, C. M., and Staten, M. L. "Automating embedded analysis capabilities and managing software complexity in multiphysics simulation, Part II: Application to partial differential equations," *Scientific Programming* Vol. 20, No. 3, 2012, pp. 327-345.

[48] Phipps, E., and Pawlowski, R. "Efficient expression templates for operator overloading-based automatic differentiation," *Recent Advances in Algorithmic Differentiation*. Springer, 2012, pp. 309-319
[49] Saad, Y., and Schultz, M. H. "GMRES: A generalized minimal residual algorithm for solving nonsymmetric linear systems," *SIAM Journal on scientific and statistical computing* Vol. 7, No. 3, 1986, pp. 856-869.
[50] Schenk, O., and Gärtner, K. "Solving unsymmetric sparse systems of linear equations with PARDISO," *Future Generation Computer Systems* Vol. 20, No. 3, 2004, pp. 475-487
[51] Karypis, G., Schloegel, K., and Kumar, V. "Parmetis: Parallel graph partitioning and sparse matrix ordering library," 1997
[52] Dannenhoffer, J.,"An Overview of the Engineering Sketch Pad," *AIAA SCITECH 2024 Forum* 2024-1315.
[53] Carlson, J.-R. "Inflow/outflow boundary conditions with application to FUN3D." 2011
[54] Park, M. A., Barral, N., Ibanez, D., Kamenetskiy, D. S., Krakos, J. A., Michal, T. R., and Loseille, A.,"Unstructured grid adaptation and solver technology for turbulent flows," *2018 AIAA aerospace sciences meeting* 2018-1103
[55] Michal, T., Krakos, J., Kamenetskiy, D., Galbraith, M., Ursachi, C.-I., Park, M. A., Anderson, W. K., Alauzet, F., and Loseille, A. "Comparing unstructured adaptive mesh solutions for the high lift common research airfoil," *AIAA journal* Vol. 59, No. 9, 2021, pp. 3566-3584
[56] Balan, A., Park, M. A., Anderson, W. K., Kamenetskiy, D. S., Krakos, J. A., Michal, T., and Alauzet, F. "Verification of anisotropic mesh adaptation for turbulent simulations over ONERA M6 wing," *AIAA Journal* Vol. 58, No. 4, 2020, pp. 1550-1565
[57] Park, M. A., Kleb, W. L., Anderson, W. K., Wood, S. L., Balan, A., Zhou, B. Y., and Gauger, N. R.,"Exploring Unstructured Mesh Adaptation for Hybrid Reynolds-Averaged Navier–Stokes/Large Eddy Simulation," *AIAA Scitech 2020 Forum* 2020-1139
[58] Park, M. A., Haimes, R., Wyman, N. J., Baker, P. A., and Loseille, A.,"Boundary representation tolerance impacts on mesh generation and adaptation," *AIAA aviation 2021 forum* 2021-2992
[59] Grasso, F., and Pettinelli, C. "Analysis of laminar near-wake hypersonic flows," *Journal of Spacecraft and Rockets* Vol. 32, No. 6, 1995, pp. 970-980.
[60] Weiss, R. F. "A new theoretical solution of the laminar, hypersonic near wake," *AIAA Journal* Vol. 5, No. 12, 1967, pp. 2142-2149.
[61] Brock, J. M., Subbareddy, P. K., and Candler, G. V. "Detached-eddy simulations of hypersonic capsule wake flow," *AIAA journal* Vol. 53, No. 1, 2015, pp. 70-80.